RSC Advances

PAPER

View Article Online
View Journal | View Issue

Cite this: *RSC Adv.*, 2024, **14**, 34883

Improved thermoelectric performance of PEDOT:PSS/Bi_2Te_3/reduced graphene oxide ternary composite films for energy harvesting applications

Vaishali Rathi, *[a] Kamal Singh, [b] K. P. S. Parmar,[b] Ranjeet K. Brajpuriya *[b] and Ashish Kumar *[bc]

We report a significant enhancement in the thermoelectric power of PEDOT by fabricating a novel ternary composite film by incorporating Bi_2Te_3 and rGO. A series of five samples of PEDOT:PSS/Bi_2Te_3/rGO ternary composite films were synthesized using a spin coating method and having different weight% (0.0, 0.1, 0.2, 0.3 wt%) of rGO in PEDOT:PSS/0.4 wt% Bi_2Te_3 mixture along with pure PEDOT:PSS sample. The Seebeck coefficient, electrical conductivity, and power factor increased in composite films compared to pure PEDOT:PSS films. Incorporating rGO enhanced charge carrier mobility because of its highly conductive network, whereas Bi_2Te_3 provided higher Seebeck coefficients owing to its inherent thermoelectric properties. PEDOT:PSS offered mechanical flexibility and a conductive matrix, facilitating effective phonon scattering and inherently lower thermal conductivity. The sample (PEDOT:PSS/0.4 wt% Bi_2Te_3/0.1 rGO wt%) demonstrated the highest electrical conductivity of 1522.4 S cm^{-1}, a Seebeck coefficient of (+) 24.7 μV K^{-1}, and a power factor of 93.16 μW m^{-1} K^{-2} at room temperature. These values represent a twelve-fold increase compared to pristine PEDOT films. A flexible, printable thermoelectric generator (TEG) was also demonstrated on polyimide substrate using inks prepared from p-type PEDOT:PSS/Bi_2Te_3/rGO and n-type PVDF/Ni NWs. The paper TEG achieved a maximum power output of 242.1 nW, with an output voltage of 9.84 mV and an output current of 49.21 μA at a temperature difference (ΔT) of 35 K. XRD, Raman spectroscopy SEM, and XPS techniques were used to understand the underlying mechanism. This novel PEDOT:PSS/Bi_2Te_3/rGO ternary composite film significantly outperforms previously reported organic thermoelectric materials. The results indicate that the combined effect of PEDOT:PSS, Bi_2Te_3, and rGO greatly enhances thermoelectric performance, offering a promising and efficient route for the application of PEDOT in advanced thermoelectric conversion processes.

Received 27th August 2024
Accepted 24th October 2024

DOI: 10.1039/d4ra06184e

rsc.li/rsc-advances

1. Introduction

Thermoelectric (TE) materials are being extensively researched and employed in various advanced devices to minimize the adverse effects of environmental pollution and address the global energy crisis in the 21st century.[1–3] The unique property of these materials is that they can directly transform thermal energy into electric power. The figure of merit (ZT) is a dimensionless factor used to determine the efficiency of the energy conversion process, as given by $(ZT = S^2\sigma)/\kappa$. Here, symbols S, σ, κ, and T represent the Seebeck coefficient, electrical conductivity, thermal conductivity and absolute temperature, respectively. To achieve optimal performance, thermoelectric (TE) materials must combine high Seebeck coefficient and electrical conductivity while exhibiting low thermal conductivity.[3] The advancements in TE application of conventional inorganic semiconductor materials, such as Bi_2Sb_3, Bi_2Te_3, and PbTe, are widely acknowledged.[2,3] Compared to their inorganic counterparts, conducting polymers promise distinct advantages of excellent flexibility, abundant availability, cost-effectiveness, light weight, and inherent low thermal conductivity when employed in waste heat harvesting.[4–6] Poly(3,4-ethylenedioxythiophene):poly (styrenesulfonate) (PEDOT:PSS) is a conducting polymer that exhibits promising characteristics for utilization in TE applications. This commercially available polymer demonstrates notable advantages such as water dispersibility, affordability, high transparency, and easy processability.[7–9] These characteristics contribute to its potential as a viable material in thermoelectrics. However, it should be noted that the TE performance exhibited by this particular polymer is significantly lower compared to its inorganic counterparts, as indicated by previous studies.[10,11]

[a]*Department of Chemistry, Applied Science Cluster, U.P.E.S., Bidholi, Dehradun, India. E-mail: vaishali25011996@gmail.com*

[b]*Department of Physics, Applied Science Cluster, U.P.E.S., Bidholi, Dehradun, India. E-mail: ranjeethjp1@gmail.com; dr.akmr@gmail.com*

[c]*Department of Physics and Astronomical Science, Central University of Jammu, Rahya-Suchani, Samba, Jammu, J&K, India*

Numerous efforts have been undertaken to enhance the TE performance of PEDOT:PSS through different methods, such as solvent post-treatment, redox state control, and filler dropping. Di-ethylene glycol (DEG), dimethyl sulfoxide (DMSO), and ethylene glycol (EG) have been identified as effective solvents for post-treatment.[12,13] The solvents have shown promising results in dissolving the PEDOT:PSS chains and effectively eliminating PSS from the PEDOT:PSS structure. As a result, a robust vander Waal bond is formed between the PEDOT particles and the PEDOT:PSS, leading to the development of distinctive surface structures. The electrical conductivity of PEDOT:PSS can be significantly improved by selectively eliminating PSS, an insulator and non-ionized dopant. The enhancement observed can be attributed to the closer proximity between PEDOT chains, which facilitates improved charge transfer.[12,13] However, the regulation of PEDOT oxidation presents challenges, as the stability of the properties in the redox state of PEDOT is not easily controlled. Moreover, the PEDOT:PSS material, known for its high conductivity, still exhibits a relatively low Seebeck coefficient.[6] This coefficient, typically quantified within the range of 14–18 $\mu V\ K^{-1}$, remains a limitation in its TE performance.[6]

Various highly conductive TE fillers have been employed as dopants to enhance the TE properties of PEDOT:PSS polymers. These fillers serve the electrical conductivity and balance the power factor (PF) notable examples of such fillers include $Ca_3Co_4O_9$,[14] Te–Bi_2Te_3,[15] Te,[16] graphene,[17] graphene oxides,[18] carbon nanotubes,[19] and reduced graphene oxide (rGO).[20] The graphene fillers exhibit superior potential due to their remarkable carrier mobility, strong mechanical characteristics, substantial-high specific area, and exceptional chemical tolerance.[21–23] Prior studies have demonstrated that when graphene and its derivatives are added to conductive polymers, the Seebeck coefficient and electrical conductivity improve. The observed enhancement has been ascribed to the energy filtering mechanism and the emergence of well-organized chains at the interfaces in the composite materials.[24,25] However, it is essential to highlight that the power factor (PF) of the PEDOT:PSS/graphene composite remains relatively low compared to inorganic TE materials. These have been attributed to the inherent characteristics of graphene, such as its low water-solubility and tendency to aggregate within the polymer matrix. Despite the strong π–π interaction between PEDOT and graphene, these factors reportedly contribute to the limited PF observed in the composite.[26] Theoretical considerations suggest that by manipulating the size of graphene structures such as nanoribbons, antidots, and nanorods, it is possible to enhance their TE figure of merit (*ZT*) by a combination of reduced thermal conductivity and an intensified energy filtering effect, both of which are inherent to smaller-sized graphene configurations.[27,28] Yong *et al.*[29] reported that the highest electrical conductivity observed was 753.8 S cm^{-1} for DMSO-doped PEDOT:PSS, which was prepared using the drop casting method.

In this work, we adopt a promising approach to enhance the electrical conductivity and Seebeck coefficient by incorporating both rGO and Bi_2Te_3 in the PEDOT:PSS films. These PEDOT:PSS/Bi_2Te_3/rGO ternary composite films fabricated by the spin coating method are aimed to bring superior electrical and thermoelectric properties of rGO and Bi_2Te_3 to PEDOT:PSS polymer host. Based on the literature, the ternary composite films mentioned above have not yet been studied. In addition, a thermoelectric generator (TEG) device consisting of p-leg PEDOT:PSS/Bi_2Te_3/rGO and n-leg PVDF/Ni NWs is also demonstrated on flexible polyimide substrates.

2. Experimental

2.1. Materials and method

PEDOT:PSS, graphite flakes, and Bi_2Te_3 were procured from Sigma-Aldrich, USA sulphuric acid, hydrochloric acid, H_3PO_4, H_2O_2, $KMnO_4$, dimethyl sulfoxide (DMSO), ethylene glycol (EG), hydrazine hydrate, acetone, ethyl alcohol, and isopropyl alcohol (IPA), DI water were purchased from Alfa Aeser, UK and Molychem, India. The chemicals utilized in the experiment were of analytical grade and were employed without any subsequent purification process.

2.2. Synthesis of reduced graphene oxide (rGO)

Graphene oxide (GO) was synthesized using the modified Hummers' method through oxidation and exfoliation of graphite sheets by the thermal treatment of the solution. The stepwise synthesis method used is elaborated as follows. Firstly, a mixture of 180 ml H_2SO_4 and 10 ml H_3PO_4 was stirred for 15–20 min at 40–45 °C. After that, 1.5 gm graphite flakes were added to the mixture with continuous stirring and $KMnO_4$ (7.5 gm) was added to the suspension very slowly at 50 °C which gave the greenish coloured solution. The solution was kept overnight in a stirrer, where the colour changed to reddish brown. After that, 100 ml DI water and 10 ml H_2O_2 were added slowly and sequentially. The mixture was left undisturbed for a period of 3–4 hours, allowing the particles to segregate at the bottom. The excess water is then carefully filtered. The resulting mixture undergoes multiple washes through centrifugation, with 1 M solution of HCl in DI water. This process is repeated several times until a gel-like substance is formed with a neutral pH, which undergoes vacuum drying at a temperature of 60 °C for 12 hours, resulting in the formation of GO powder. Again, hydrazine hydrate was used as a reducing agent for the GO suspension. The mixture undergoes sonication for 6 hours in order to transition from GO to rGO. The rGO suspension underwent filtration, followed by multiple washes with ethanol and DI water, before being collected for future use.

2.3. Preparation of PEDOT:PSS/Bi_2Te_3/rGO ternary composite film

PEDOT:PSS film was fabricated utilizing the drop-casting technique. A dispersed solution of PEDOT:PSS and Bi_2Te_3 were prepared by separately dissolving the components in DMSO and ethanol, respectively. The amount of DMSO and ethanol are the same throughout the manuscript. The solution was treated with ultrasonication for a duration of 1 h. The experimental procedure involved the combination of an optimal quantity of

PEDOT:PSS solution with a 0.4 wt% Bi_2Te_3 solution, which was subsequently subjected to stirring for 2 hours at room temperature (RT). The 0.4 wt% Bi_2Te_3 ratio was selected based on our earlier investigations.[30] Separately, a solution of rGO in ethanol was ultrasonicated to get a homogenously dispersed solution. Appropriate amounts of this rGO solution were added to PEDOT:PSS/0.4 wt% Bi_2Te_3 solution to get homogenous solutions containing different weight % (0.1, 0.2, 0.3 wt%) of rGO. Glass substrates (1×1 cm^2) underwent a thorough cleaning process involving sequential ultrasonic treatment in deionized (DI) water, IPA, and acetone for a duration of 15 each. Ternary composite films of PEDOT:PSS/Bi_2Te_3/rGO were synthesized employing a spin coating method (1000 rpm followed by 2000 rpm) and subsequent drying of the resultant composite films in a vacuum oven at 70 °C for five hours. The thickness of the films was measured and found to be approximately 8–10 μm. The schematic diagram for the synthesis procedure is depicted in Fig. 1. Pure PEDOT:PSS and PEDOT:PSS/0.4 wt% Bi_2Te_3 films were also synthesized using the identical procedure for comparative analysis. A total of five film samples were used for various characterisations. The sample notations (S0, S1, S2, S3, and S4) and compositions are listed in Table 1. For n-type thermoelectric material, polyvinylidene fluoride and nickel nanowire (PVDF/Ni NW) solution was prepared and will be discussed separately.

2.4. Characterizations

The crystal structure of the ternary composite film was analyzed using the grazing incidence X-ray diffraction (GIXRD, Malvern Panalytical, USA) technique. The measurements were performed with a Cu Kα radiation source ($\lambda = 1.5406$ Å) at an applied current of 40 mA and voltage of 45 kV. The investigation examined the conformational changes occurring in PEDOT and PSS composite films. A Raman spectrum was obtained using a green laser emitting light at 532 nm to produce excitation (RI, India). The X-ray Photoelectron Spectroscopy (XPS), analysis

Table 1 The sample name and compositions used in the present investigation

Sample name	Notation
PEDOT:PSS (pristine)	S0
PEDOT:PSS/0.4 wt% Bi_2Te_3	S1
PEDOT:PSS/0.4 wt% Bi_2Te_3/0.1 wt%rGO	S2
PEDOT:PSS/0.4 wt% Bi_2Te_3/0.2 wt%rGO	S3
PEDOT:PSS/0.4 wt% Bi_2Te_3/0.3 wt%rGO	S4

was conducted utilizing a (PHI 5000 Versa probe Scanning Microscope, ULVAC-PHI Inc., USA). The high-resolution spherical capacitor energy analyser thoroughly examines various energy levels, allowing for a detailed evaluation of specific elements through XPS full spectrum analysis. The spectra were acquired through the exposure of the samples to incident radiation emitted by a monochromatic Al-Kα X-ray source operating at an energy level of 1486.6 eV. The XPS data was analysed, and peak deconvolution was carried out to inform the chemical and electronic states of the constituent elements and bonds in the prepared composite films. The composite films were analysed using a scanning electron microscope (SEM) to examine their morphology and microstructure. The Seebeck coefficient was determined using a custom experimental setup developed in-house.[31] A four-probe current–voltage (I–V) measurement technique was employed to determine the electrical conductivity of the sample.

3. Result and discussion

3.1. XRD

The X-ray diffraction patterns of PEDOT:PSS, PEDOT:PSS/Bi_2Te_3, and PEDOT:PSS/Bi_2Te_3/rGO composite films are displayed in Fig. 2. S0 sample shows two distinct broad diffraction peaks at 17° and 26°, corresponding to lattice spacing of around 5.0 and 3.4 Å, indicating the mostly amorphous nature of

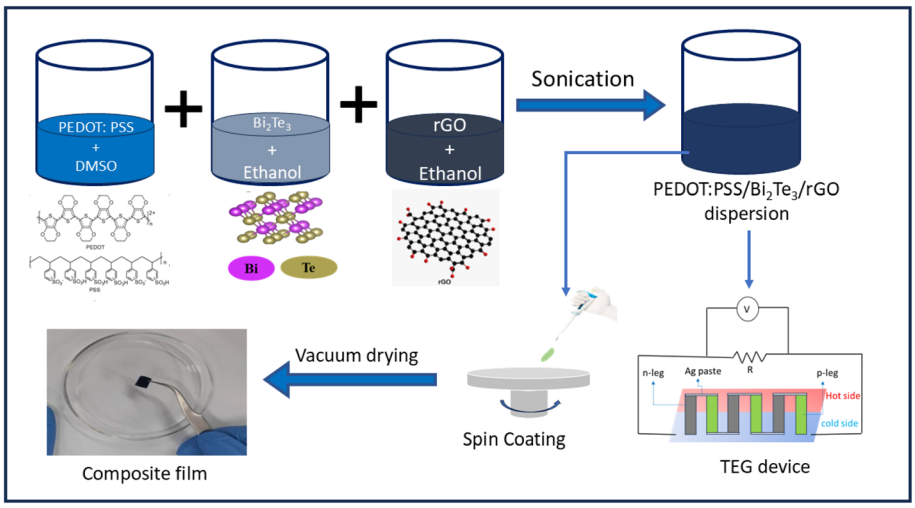

Fig. 1 The schematic illustrates the process flow for preparing the PEDOT:PSS/Bi_2Te_3/rGO ternary composite film using the spin coating method.

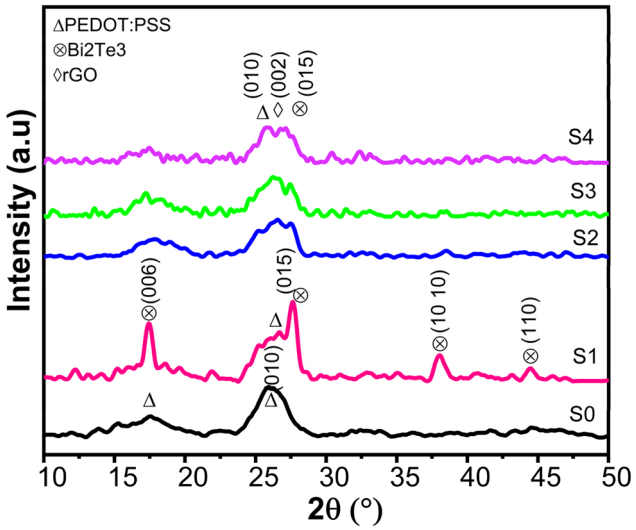

Fig. 2 GIXRD of Raman spectra of S0 (PEDOT:PSS), S1 (PEDOT:PSS/Bi_2Te_3), and S2, S3, and S4 (PEDOT:PSS/Bi_2Te_3/rGO) composite films.

PEDOT:PSS film. The diffraction peak at 26° is attributed to the interplanar distance (d_{010}) associated with the π–π stacking arrangement of the aromatic rings in PEDOT. In comparison, peaks at 17° are reported to be caused by the π–π stacking distance of PSS.[32,33] The addition of Bi_2Te_3 in the PEDOT:PSS matrix results in several other peaks in the experimental data in sample S1. The observed additional characteristic peaks at 2θ values of 17.7°, 27°, 38°, and 44° are attributed to the crystallographic (006), (015), (10 10), and (110) planes of Bi_2Te_3, respectively. These observed peaks agree with the reference data (JCPDS No. 15-0863).[34] For samples S2, S3, and S4, another peak is observed at 25°, which is reported to the (002) plane of rGO.[35] Also, with the increase in wt% of rGO (samples S2, S3, and S4), the intensity of two distinctive peaks at 26°and 27° weaken. This suggests that the aggregation of rGO plays a role in this phenomenon. The interaction between aggregated rGO and PEDOT chains leads to the destruction of PSS.[36] This behaviour is also observed in the SEM images.

3.2. SEM

Fig. 3(a)–(e) shows the scanning electron microscopy (SEM) images of composite films. SEM micrographs of the S0 film (Fig. 3(a)) show a consistent and homogenous surface morphology. After adding Bi_2Te_3 in S1 (Fig. 3(b)) and rGO in S2, some bulge-type structures appear on the film surface, as shown in Fig. 3(c) and (d). The presence of several π bonds within the structure of PEDOT:PSS is a well-established fact. Also, it is widely reported that rGO possesses a significant number of π bonds, enabling their efficient incorporation into a PEDOT:PSS matrix through strong π–π interactions with PEDOT chains.[37] With the further addition of rGO in PEDOT:PSS agglomeration occurs in films, as is evident in Fig. 3(e), which corresponds to sample S4. The rGO material exhibits exclusive π–π interactions with PEDOT chains while displaying relatively weaker interactions with PSS chains.[37] The rGO strong multiphase interactions may cause the PEDOT and PSS chains phase to separate, forming the grains on the surfaces of ternary composite PEDOT:PSS/Bi_2Te_3/rGO/.[38,39]

3.3. Raman spectroscopy

The Raman spectra provide insights into carbon-based materials' defects and disordered structures. Fig. 4 displays the

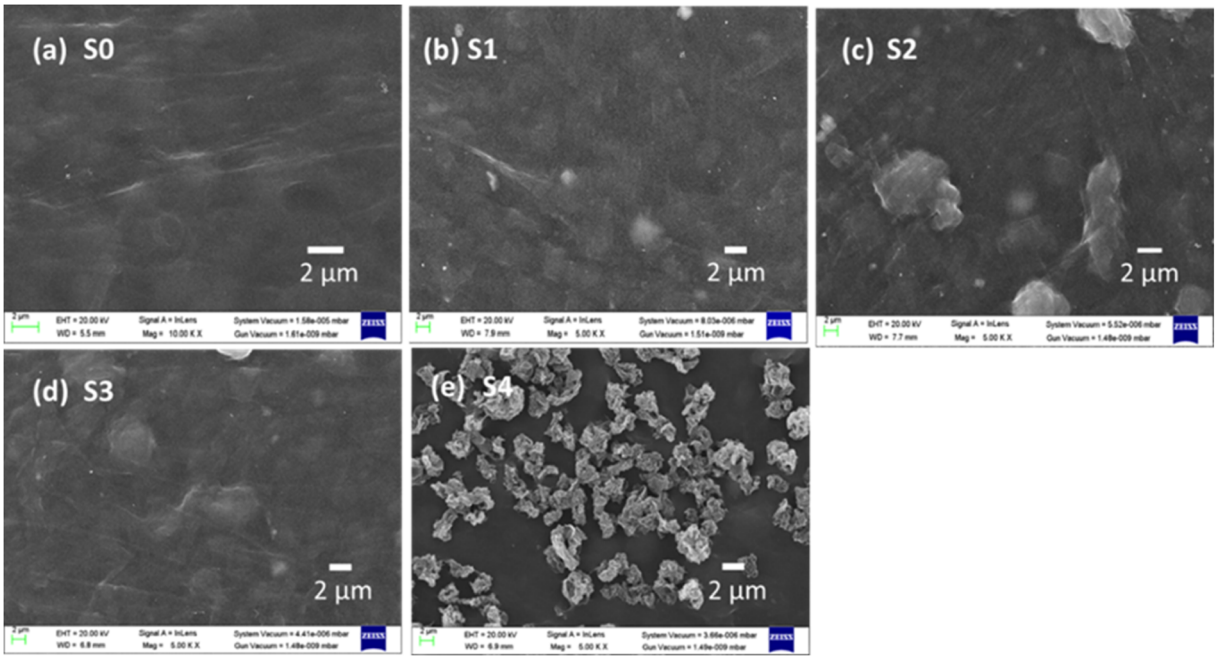

Fig. 3 (a)–(e) Represents SEM images of samples S0 (PEDOT:PSS), S1 (PEDOT:PSS/Bi_2Te_3), and S2, S3, and S4 (PEDOT:PSS/Bi_2Te_3/rGO) composite films, respectively.

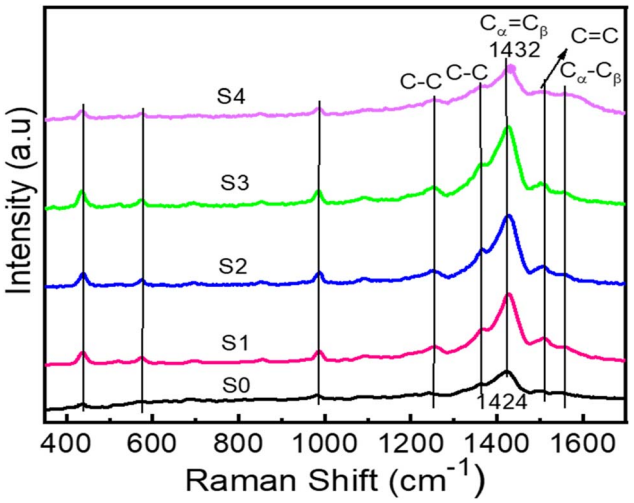

Fig. 4 Raman spectra of S0 (PEDOT:PSS), S1 (PEDOT:PSS/Bi_2Te_3), and S2, S3, and S4 (PEDOT:PSS/Bi_2Te_3/rGO) composite films. The shifting of the C=C symmetric stretching vibrational mode peak at 1424 cm^{-1} to higher wavenumber is attributed to the π–π interaction between the electron-rich rGO and the aromatic structures of PEDOT.

measured Raman spectra of all films. The G band in carbon materials can be ascribed to the vibrational modes of sp^2-bonded carbon atoms. In contrast, the D band signifies the vibrational modes of carbon atoms that possess dangling bonds. The presence of the D peak also means the existence of defects and disordered structures within carbon-based materials.[40]

The Raman spectra of all samples exhibit noticeable characteristic peaks, including the presence of weak peaks associated with C–C bond stretching at 1251 cm^{-1}, C–C stretching vibrational band at 1363 cm^{-1}, and the dominant band at 1424 cm^{-1} associated with C=C symmetric stretching, C=C asymmetric stretching at 1507 cm^{-1} and antisymmetric stretching at 1557 cm^{-1}. The band at 986 cm^{-1} and 574 cm^{-1} corresponds to the oxyethylene ring deformation vibrations.[41,42] The observed band at 436 cm^{-1} can be attributed to incorporating the SO_3^- ion from PSS units, which acts as a dopant in the PEDOT material.[43] It can be noticed that the C=C symmetric stretching vibrational mode peak at 1424 cm^{-1} of sample S0 is shifting to a higher wavenumber of approximately 1432 cm^{-1}, with the addition of rGO. The shift is also reported in the literature and is attributed to the π–π interaction between the electron-rich rGO and the aromatic structures of PEDOT.[26] From analysis of the Raman spectra, it is evident that there is a significant interaction between rGO and PSS and PEDOT chains. This interaction leads to the separation of the PEDOT:PSS phase and promotes the alignment of PEDOT in a structured manner, as also reported elsewhere.[44]

3.4. XPS

XPS is a highly effective measurement technique for identifying the elements present and their chemical bonding with other elements. For XPS, only selected samples were used for comparison. Fig. 5 exhibits the XPS spectra of pristine PEDOT:PSS (S0), binary composite PEDOT:PSS/Bi_2Te_3 (S1) and ternary composite PEDOT:PSS/Bi_2Te_3/0.1rGO (S2) samples. Analysis of C (1s), O (1s), S (2p), Bi (4f), and Te (3d) peaks have been carried out. The C (1s) peak, with a central position at 284.6, exhibits a broad and asymmetric shape. A deconvolution fitting procedure involving the utilization of distinct peaks is shown in Fig. 5(A)–(C). The observed peaks in the C (1s) spectrum of S2 can be attributed to distinct chemical bonds, namely, the C–C and C–H bonds at 284.6 eV, C–S at 285.1 eV bond, C=C–O bond at 286.1 eV, and C–O–C bond at 287.1 eV, respectively.[45,46] The result obtained in this study demonstrates a significant degree of accordance with the findings reported in the previous research.[45–47] The incorporation of rGO in the structure shows an apparent π–π interaction between PEDOT chains and rGO, emphasizing favourable compatibility between the rGO and PSS chains.[47] The O (1s) spectra in Fig. 5(D)–(F) demonstrate two peaks with different binding energy. The observed peaks indicate the presence of an O atom within the PEDOT chain, localized within a higher B.E. range at approximately 533 eV. In contrast, the O-atoms within the PSS chain demonstrate distinct peaks in a lower B.E. range at 531.5 eV, as shown in Fig. 5. The S0 film shows two discernible peaks (Fig. 5(G)), which can be attributed to the 2p orbitals of sulfur. This observation provides evidence for the existence of sulfur atoms within the film. The observed lower energy peaks at 164.9 and 163.7 eV can be ascribed to the presence of S atoms within the PEDOT chain. Conversely, the higher B.E. peaks at 168.9 and 167.7 eV indicate the sulfur atom within the PSS chain.[42,48,49] In Fig. 5(H) and (I) for samples binary (S1) and ternary (S2) composite film, additional peaks were observed at 159.8 eV and 165.5 eV in the binary ternary composite film, indicating the presence of Bi_2O_3 and Bi_2Te_3, respectively. The presence of Bi(4f) has been observed in the binary (S1) and ternary composite film (S2), suggesting its incorporation within the film. Fig. 5(J) and (K) shows the XPS spectra of the $Te_{5/2}$ electron orbital, which reveal the presence of two distinct subpeaks at energy levels of 573.2 and 576.7 eV, respectively. Similarly, the $Te_{3/2}$ orbital shows two distinct peaks located at 583.5 and 586.9 eV. The observed spectral peaks at 576.7 and 586.9 eV suggest the existence of tellurium oxide (TeO_2) on the surface being examined in the ternary composite films. Extra peaks were identified in the context of carrying out the 3d spectral analysis. These peaks can be assigned to the existence of secondary oxide.[50]

3.5. Thermoelectric properties of PEDOT:PSS-based ternary composite film

3.5.1. Electrical properties. The four-probe method examined the temperature-dependent sheet resistance (R_S) and electrical conductivity (σ) for all samples. Studies have shown that the conductivity of PEDOT:PSS can be enhanced by adding Bi_2Te_3 in PEDOT:PSS composite film.[51,52] This enhancement in conductivity has been observed to be 2–3 orders of magnitude. Fig. 6(a) depicts the change in conductivity of S0, S1, S2, S3, and S4 composite films as a function of temperature. The electrical conductivity in all the samples increases with increasing

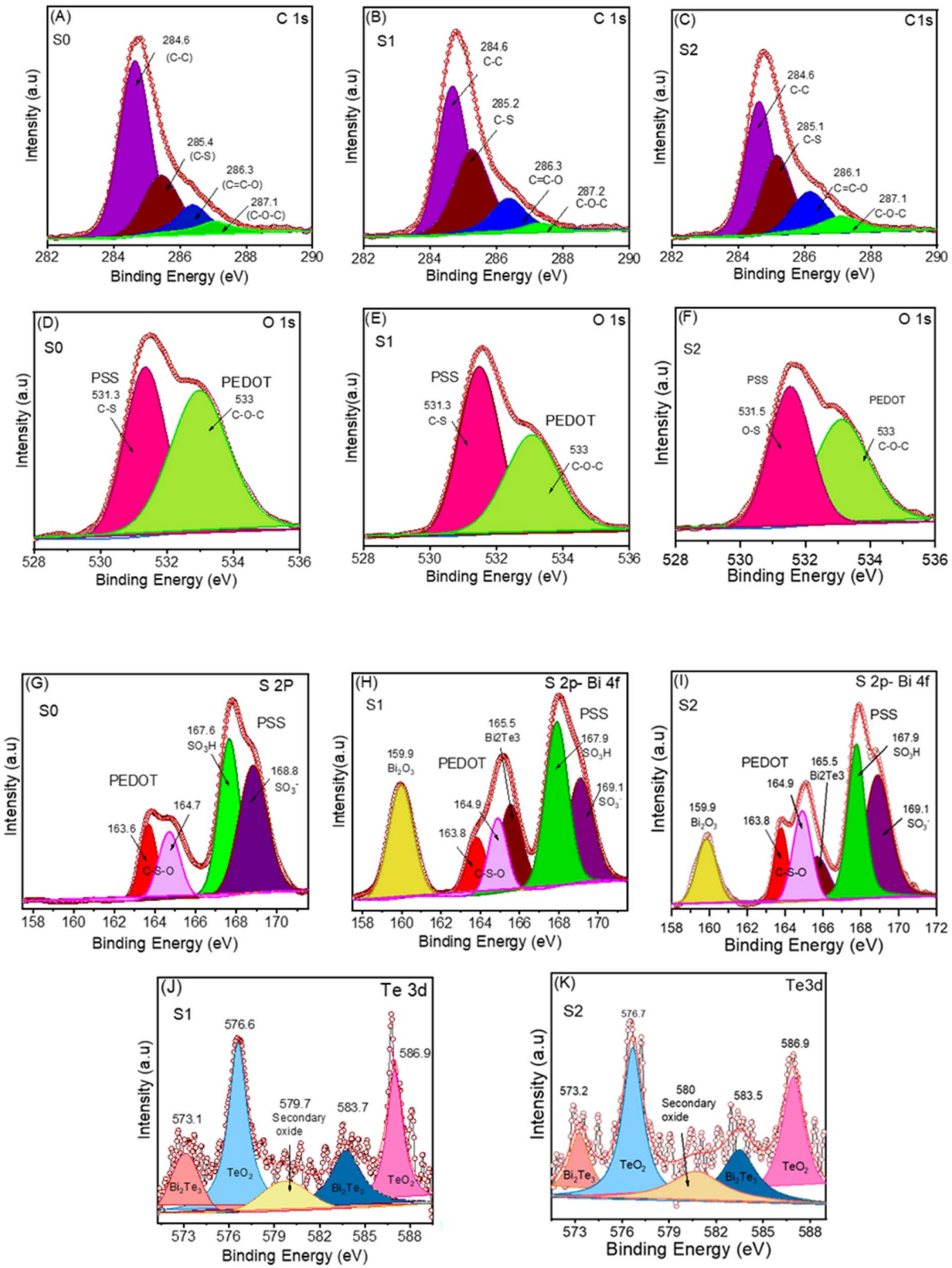

Fig. 5 XPS spectra of PEDOT:PSS (S0), PEDOT:PSS/0.4% Bi_2Te_3 (S1) and PEDOT:PSS/0.4% Bi_2Te_3/0.1% rGO (S2) composite films. Figures (A)–(C) show XPS deconvolution for C (1s) peak in S0, S1, and S2 samples, respectively. Figures (D)–(F) compare the binding energies of the O (1s) peak for S0, S1, and S2 samples. Figures (G)–(I) show the sulphur (2p) peak in S0, sulphur (2p) and Bi (4f) peaks in S1 and S2 samples, respectively. Lastly, figures (J) and (K) compare XPS binding energies deconvolution of Te (3d) peak in S1 and S2 samples, respectively.

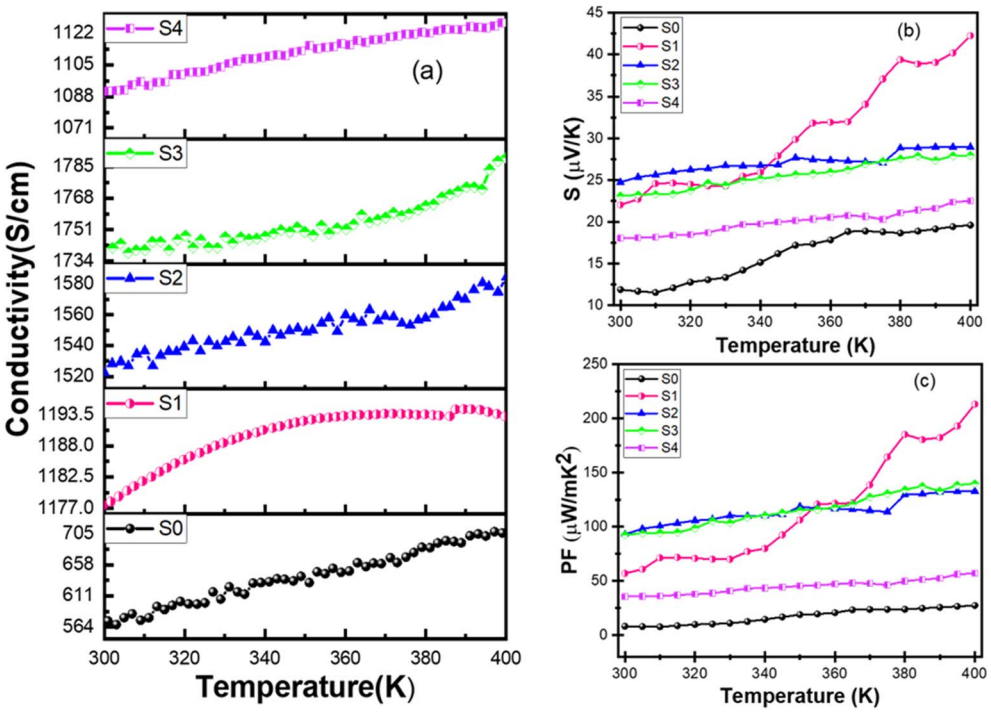

Fig. 6 (a) Measured electrical conductivity, (b) Seebeck coefficient, and (c) power factor of PEDOT:PSS (S0), PEDOT:PSS/0.4% Bi_2Te_3 (S1) and PEDOT:PSS/0.4% Bi_2Te_3/0.1% rGO (S2) composite films.

temperature, indicating the semiconductor nature of the composites formed. The electrical conductivity of the pure PEDOT:PSS film (S0) was 573.12 S cm^{-1} at room temperature. The addition of Bi_2Te_3 in PEDOT:PSS film (S1) increased the electrical conductivity value of 1177.5 S cm^{-1}. A previous study also reported the electrical conductivity and Seebeck coefficient of PEDOT:PSS/Bi_2Te_3 samples with varying concentrations of Bi_2Te_3.[30] When rGO was added to the composite, the room temperature conductivity was observed at 1522.4 S cm^{-1}, 1741.1 S cm^{-1} and 1076.6 S cm^{-1} for S2 (0.1 wt% rGO), S3 (0.2 wt% rGO), and S4 (0.3 wt% rGO) films, respectively. The highest electrical conductivity was observed for S3 and was more than 3.5 times of S0 at 300 K. The electrical conductivity of the nanocomposites exhibits a significant correlation of rGO within the PEDOT:PSS matrix. The incorporation of rGO at a concentration up to 0.3 wt% within the PEDOT:PSS matrix leads to an enhancement of π–π conjugation along the polymer chain. This phenomenon generates a significant population of charge carriers that exhibit delocalized behaviour, enabling their facile movement between energetically favourable sites.[52]

3.5.2. Seebeck coefficient measurement. Fig. 6(b) shows the measured Seebeck coefficient values of all samples. All samples exhibited a positive Seebeck coefficient, which displayed an upward trend with rising temperature, resembling the observed behaviour in literature.[25,53] All the rGO composite films exhibit higher Seebeck coefficients at 300 K temperature than the value of 11.8 μV K^{-1} observed in pure PEDOT:PSS (S0), and 22 μV K^{-1} in PEDOT:PSS/0.4% Bi_2Te_3 (S1) samples. The S2 sample showed the highest value of the Seebeck coefficient, measuring 24.7 μV K^{-1} at 300 K. The Seebeck coefficient S3 sample showed a similar magnitude (23.07 μV K^{-1}) and trend as that of S2. In comparison, S4 samples exhibit a moderate Seebeck coefficient value of 18.05 μV K^{-1} at the same temperature (300 K). The observation indicates that less carriers are transported in the interface when higher filler contents are present. This occurrence can be attributed to the inefficiency of the relation between the PEDOT chain and fillers, as previously reported in the literature.[26] The Seebeck coefficients of the composite film exhibit a positive correlation with temperature, indicating an increase as temperature rises. This observation implies an energy filtration effect from combining organic and inorganic materials. The observed phenomenon involves an accompanying reduction in the electrical conductivity and Seebeck coefficient as the concentration of rGO is enhanced. The observed decrease in the Seebeck coefficient values for further higher concentrations of rGO can be predominantly attributed to eliminating energy barriers between the polymer and inorganic materials.[54]

Furthermore, power factor (PF) values were determined for as prepared PEDOT:PSS (pure) and different weight percentages of rGO added in PEDOT:PSS/0.4% Bi_2Te_3, namely, S0, S1, S2, S3, and S4 respectively resulting in PF values of 8.12 μW m^{-1} K^{-2}, 57.04 μW m^{-1} K^{-2}, 93.16 μW m^{-1} K^{-2}, 92.6 μW m^{-1} K^{-2}, 35.5 μW m^{-1} K^{-2}, respectively at 310 K as shown in Fig. 6(c). The calculated values of PF exhibit similarities to the σ and S patterns for different compositions, as shown in Table 2. It can be seen clearly that the ternary composite film S2 exhibits the highest PF value, 93.16 μW m^{-1} K^{-2} at 300 K, making it a highly appropriate composition for TE applications. A comparison of results from the present investigation with the literature clearly

Table 2 Comparison of thermoelectric parameters of PEDOT:PSS/Bi_2Te_3/rGO composite films at room temperature with other's work

Samples	Composite method	Electrical conductivity (S cm^{-1})	Seebeck coefficient (μV K^{-1})	Power factor (μW m^{-1} K^{-2})	References
Bi_2Te_3/rGO	Hydrothermal	42	−187	1.46	55
Bi_2Te_3 alloy NS/PEDOT:PSS	Drop casting/solution casting	1295.21	47.5	32.26	10
PEDOT:PSS/rGO	*In situ* polymerization	637	24.375	45.7	56
PEDOT NW/Bi_2Te_3	Hydrothermal	249.5	13.3	9.06	57
PEDOT:PSS/rGO	Wet chemical method	1160	12.5	32.6	25
PEDOT:PSS/graphene	Spin coating method	32.13	58.7	11.09	24
PEDOT:PSS/Bi_2Te_3	Physical mixing method	421	18.6	9.9	51
Chalcopyrite/PEDOT:PSS/graphene	Drop casting	77.4	−61.7	23.4	58
PEDOT:PSS/0.4 wt% Bi_2Te_3	Spin coating	1177.57	22	57.04	Present study
PEDOT:PSS/0.4 wt% Bi_2Te_3/0.1 wt% rGO	Spin coating	1522.4	24.7	93.16	Present study
PEDOT:PSS/0.4 wt% Bi_2Te_3/0.2 wt% rGO	Spin coating	1738.8	23.07	92.6	Present study
PEDOT:PSS/0.4 wt% Bi_2Te_3/0.3 wt% rGO	Spin coating	1089	18.05	35.53	Present study

indicates better performance of our ternary composite films for thermoelectric applications.

3.5.3. Thermoelectric generator (TEG) device performance. We prepared inks of p-type PEDOT:PSS/0.4 wt%Bi_2Te_3/0.1 wt% rGO and n-type PVDF/Ni NWs solutions. The synthesis and characterisation of n-type PVDF/Ni NWs solutions for thermoelectric application will be part of a separate study. A thermoelectric generator (TEG) demonstration device was fabricated using two inks on the flexible polyimide substrate. Fig. 1 shows the schematic of TEG devices. The output voltage as a function of the temperature difference ΔT varies from 10 to 35 K, and the open circuit voltage due to the Seebeck effect increases linearly with increasing the temperature difference of ΔT between the hot and cold ends of the TE module. An output voltage of 9.84 mV at $\Delta T = 35$ K and the maximum power output of 242.16 nW is attained with the load resistance of 100 Ω at $\Delta T = 35$ K.

4. Conclusions

In summary, PEDOT:PSS/Bi_2Te_3/rGO ternary composite films with varying concentrations of rGO were fabricated using the spin coating method. This study reports significantly enhanced thermoelectric (TE) properties of PEDOT:PSS by incorporating Bi_2Te_3 and rGO, providing a promising pathway for high-efficiency TE conversion. The structural and morphological characteristics of the composites were thoroughly evaluated using various analytical techniques. Raman spectroscopy revealed a notable interaction between PEDOT:PSS and rGO, where this interaction induces a structural transformation. This transformation is advantageous for linear structures as it increases conductivity. Strong intermolecular interactions between organic and inorganic chains through π–π bonding and between rGO and PSS chains *via* hydrophilic groups result in PEDOT and PSS chains' decoupling and phase separation. The thermoelectrical analysis of PEDOT:PSS/Bi_2Te_3/rGO composites showed remarkable improvements in electrical conductivity and the Seebeck coefficient. At room temperature, the PEDOT:PSS/0.4% Bi_2Te_3/0.1% rGO (S2) ternary composite films exhibited the highest electrical conductivity (1522.4 S cm^{-1}), Seebeck coefficient (24.7 μV K^{-1}), and power factor (PF) (93.16 μW m^{-1} K^{-2}). The PF of the optimized ternary composite concentration showed a significant increase of 5–6 folds compared to pure PEDOT:PSS (S0) samples. A thermoelectric generator (TEG) consisting of three pairs of p-leg PSS/0.4% Bi_2Te_3/0.1% rGO and n-leg PVDF/Ni NWs was also fabricated. The maximum power output of 242.1 nW was achieved with an output voltage of 9.84 mV at $\Delta T = 35$ K. These findings highlight the notable improvement in electrical conductivity and Seebeck coefficient, underscoring the potential of PEDOT:PSS in advanced applications such as energy harvesting and waste heat recovery. Considering the demand for cost-effective, flexible, lightweight, and environmentally friendly materials with outstanding TE performance, the composite films examined in this study exhibit significant potential as viable candidates for high TE performance and solid-state devices. The TEG constructed with this material demonstrated commendable performance, indicating its potential

applicability in practical scenarios such as wearable electronics, energy harvesting from waste heat, and portable power sources for compact electronics devices.

Author contributions

Vaishali Rathi: conceptualization, investigation, formal analysis, writing – original draft preparation, writing – reviewing and editing, visualization. Kamal Singh: investigation, writing – reviewing and editing. K. P. S. Parmar: supervision, investigation, writing – reviewing and editing. Ranjeet K. Brajpuriya: supervision, investigation writing – reviewing and editing. Ashish Kuma: supervision, resources, writing – original draft preparation, writing – reviewing and editing.

Conflicts of interest

The authors declare that there is no conflict and competing interest that could have appeared to influence the paper.

Acknowledgements

Vaishali Rathi would like to acknowledge UPES, Dehradun, for providing a research fellowship. Ashish Kumar would like to acknowledge the SEED grant from UPES and financial support provided by the SERB, India, under the SRS scheme. The authors also acknowledge the research facilities accessed in the Central Instrumentation Centre (CIC) of UPES, Dehradun.

References

1 S. Twaha, J. Zhu and Y. Yan, Bo. Li, *Renewable Sustainable Energy Rev.*, 2016, **65**, 698–726.
2 G. Tan, L.-D. Zhao and M. Kanatzidis, *Chem. Rev.*, 2016, **116**(19), 12123–12149.
3 L.-D. Zhao, S.-H. Lo, Y. Zhang, H. Sun, G. Tan, C. Uher, C. Wolverton, V. P. Dravid and M. Kanatzidis, *Nature*, 2014, **508**(7496), 373–377.
4 X. Hu, G. Chen and X. Wang, *Compos. Sci. Technol.*, 2017, **144**, 43–50.
5 K. Xu, G. Chen and D. Qiu, *J. Mater. Chem. A*, 2013, **1**(40), 12395–12399.
6 M. He, F. Qiu, Z. Lin and E. Science, *Energy Environ. Sci.*, 2013, **6**(5), 2011352–2011361.
7 D. Yoo and J. Kim, *Nano Res.*, 2014, **7**, 717–730.
8 J. Luo, D. Billep, T. Waechtler, T. Otto, M. Toader, O. Gordan, E. Sheremet, J. Martin, M. Hietschold and D. Zahn, *J. Mater. Chem. A*, 2013, **1**(26), 7576–7583.
9 S. K. Yee, N. E. Coates, A. Majumdar, J. J. Urban and R. Segalman, *Phys. Chem. Chem. Phys.*, 2013, **15**(11), 4024–4032.
10 Y. Du, K. Cai, S. Chen, P. Cizek and T. Lin, *ACS Appl. Mater. Interfaces*, 2014, **6**(8), 5735–5743.
11 B. Zhang, J. Sun, H. Katz, F. Fang and R. Opila, *ACS Appl. Mater. Interfaces*, 2010, **2**(11), 3170–3178.
12 G.-H. Kim, L. Shao, K. Zhang and K. Pipe, *Nat. Mater.*, 2013, **12**(8), 719–723.
13 Y. Xia and J. Ouyang, *J. Mater. Chem.*, 2011, **21**(13), 4927–4936.
14 C. Liu, F. Jiang, M. Huang, B. Lu, R. Yue and J. Xu, *J. Electron. Mater.*, 2011, **40**, 948–952.
15 E. J. Bae, Y. H. Kang, K.-S. Jang, C. Lee and S. Cho, *Nanoscale*, 2016, **8**(21), 10885–10890.
16 A. Sahu, B. Russ, N. C. Su, J. D. Forster, P. Zhou, E. S. Cho, P. Ercius, N. E. Coates, R. A. Segalman and J. Urban, *J. Mater. Chem.*, 2017, **5**(7), 3346–3357.
17 Y. Chen, J. Xu, Y. Yang, S. Li, W. Yang, T. Peng, X. Mao and Y. Zhao, *J. Mater. Sci.: Mater. Electron.*, 2015, **26**, 8292–8300.
18 J. C. Yu, J. I. Jang, B. R. Lee, G.-W. Lee, J. T. Han and M. Song, *ACS Appl. Mater. Interfaces*, 2014, **6**(3), 2067–2073.
19 W. Wang, M. A. Ruderer, E. Metwalli, S. Guo, E. M. Herzig, J. Perlich and P. Müller-Buschbaum, *ACS Appl. Mater. Interfaces*, 2015, **7**(16), 8789–8797.
20 K. Jo, T. Lee, H. J. Choi, J. H. Park, D. J. Lee, D. W. Lee and B. Kim, *Langmuir*, 2011, **27**(5), 2014–2018.
21 K. S. Novoselov, A. K. Geim, S. V. Morozov, D. E. Jiang, Y. Zhang, S. V. Dubonos, I. Grigorieva and A. Firsov, *Science*, 2004, **306**(5696), 666–669.
22 A. K. Geim, *Science*, 2009, **324**(5934), 1530–1534.
23 L. L. Zhang, R. Zhou and X. S. Zhao, *J. Mater. Chem.*, 2010, **20**(29), 5983–5992.
24 G. H. Kim, D. H. Hwang and S. Woo, *Phys. Chem. Chem. Phys.*, 2012, **14**(10), 3530–3536.
25 F. Li, K. Cai, S. Shen and S. Chen, *Synth. Met.*, 2014, **197**, 58–61.
26 J. Xiong, F. Jiang, H. Shi, J. Xu, C. Liu, W. Zhou, Q. Jiang, Z. Zhu and Y. Hu, *ACS Appl. Mater. Interfaces*, 2015, **7**(27), 14917–14925.
27 S. Zhou, Y. Guo and J. Zhao, *Phys. Chem. Chem. Phys.*, 2016, **18**(15), 10607–10615.
28 Y. Yan, Q.-F. Liang, H. Zhao, C.-Q. Wu and B. Li, *Phys. Lett. A*, 2012, **376**(35), 2425–2429.
29 Y. Du, K. F. Cai, P. Cizek and T. Lin, *ACS Appl. Mater. Interfaces*, 2014, **6**(8), 5735–5743.
30 V. Rathi, K. Singh, K. P. S. Parmar, R. K. Brajpuriya and A. Kumar, *Org. Electron.*, 2024, **133**, 107103.
31 A. Kumar, A. Patel, S. Singh, A. Kandasami and D. Kanjilal, *Rev. Sci. Instrum.*, 2019, **90**(10), 104901.
32 K. Aasmundtveit, E. Samuelsen, L. Pettersson, O. Inganäs, T. Johansson and R. Feidenhans, *Synth. Met.*, 1999, **101**(1–3), 561–564.
33 N. Kim, B. H. Lee, D. Choi, G. Kim, H. Kim, J.-R. Kim, J. Lee, Y. H. Kahng and K. Lee, *Phys. Rev. Lett.*, 2012, **109**(10), 106405.
34 Y. Du, J. Li, J. Xu and P. Eklund, *Energies*, 2019, **12**(12), 2430.
35 H. Maharana, P. Kumar Rai and A. Basu, *J. Mater. Sci.*, 2017, **52**, 1089–1105.
36 A. Giuri, S. Masi, S. Colella, A. Listorti, A. Rizzo, A. Kovtun, S. Dell'Elce, A. Liscio and C. Esposito Corcione, *Polym. Eng. Sci.*, 2017, **57**(6), 546–552.
37 Y. Li, X. Liu, J. Wang, H. Liu, S. Li, Y. Hou, W. Wan, W. Xue, N. Ma and J. Zhang, *J. Phys. Chem. C*, 2016, **120**(45), 26004–26011.

38 X. Wu, J. Liu, D. Wu, Y. Zhao, X. Shi, J. Wang, S. Huang and G. He, *J. Mater. Chem. C*, 2014, **2**(20), 4044–4050.
39 A. Kanwat and J. Jang, *Mater. Res. Bull.*, 2016, **74**, 346–352.
40 D. P. Kepić, Z. M. Marković, S. P. Jovanović, D. B. Peruško, M. D. Budimir, I. D. Holclajtner-Antunović, V. B. Pavlović and B. Marković, *Synth. Met.*, 2014, **198**, 150–154.
41 S. Garreau, G. Louarn, J. P. Buisson, G. Froyer and S. Lefrant, *Macromolecules*, 1999, **32**, 6807–6812.
42 H. Park, S. H. Lee, F. S. Kim, H. H. Choi, I. W. Cheong and J. H. Kim, *J. Mater. Chem. A*, 2014, **2**(18), 6532–6539.
43 S. Kumar, N. Kurra and H. N. Alshareef, *J. Mater. Chem. C*, 2016, **4**(1), 215–221.
44 Y. Seol, T. Trung, O. Yoon, I. Sohn and N. Lee, *J. Mater. Chem.*, 2012, **22**(45), 23759–23766.
45 D. B. Cairns, S. P. Armes, M. M. Chehimi, C. Perruchot and M. Delamar, *Langmuir*, 1999, **15**(23), 8059–8066.
46 X. Zhao, M. Dong, J. Zhang, Y. Li and Q. Zhang, *Nanotechnology*, 2016, **27**(38), 385705.
47 F. Du, N.-N. Cao, Y. Zhang, P. Fu, Y. Wu, Z. Lin, R. Shi, A. Amini and C. Cheng, *Sci. Rep.*, 2018, **8**(1), 6441.
48 Z. Guo, J. Tang, J. Yao and Y. Li, *Polym. Chem.*, 2024, **15**(21), 2191–2198.
49 Y. Li, H. Xiang, J. Wang, B. Gao, J. Tang, C. Xiao, X. Wang and F. Wang, *J. Mater. Chem. A*, 2022, **10**(43), 23165–23174.
50 J. Yadav, M. D. Anoop, N. Yadav, N. S. Rao, F. Singh, T. Ichikawa, A. Jain, K. Awasthi, R. Singh and M. Kumar, *J. Mater. Sci.: Mater. Electron.*, 2023, **34**(3), 175.
51 H. Song, C. Liu, H. Zhu, F. Kong, B. Lu, J. Xu, J. Wang and F. Zhao, *J. Electron. Mater.*, 2013, **42**, 1268–1274.
52 S. Khasim, A. Pasha, N. Badi, M. Lakshmi and Y. Mishra, *Nano Energy*, 2020, **10**(18), 10526–10539.
53 D. Ding, F. Sun, f. xia and Z. Tang, *Nanoscale Adv.*, 2020, **2**, 3244–3251.
54 W. S. Kim, G. Anoop, I. Jeong, H. Lee, H. B. Kim, S. H. Kim, G. W. Goo, H. Lee, H. J. Lee, C. Kim, J. H. Lee, B. S. Mun, J. Park, E. Lee and J. Jo, *Nano Energy*, 2020, **67**, 104207.
55 C. Kulsi, M. Mitra, K. Kargupta and D. Banerjee, *J. Mater. Sci.: Mater. Electron.*, 2019, **30**, 1850–1860.
56 D. Yoo and J. Kim, *Nano Res.*, 2014, **7**, 717–730.
57 Z. Tian, H. Liu, N. Wang, Y. Liu and X. Zhang, *ACS Appl. Mater. Interfaces*, 2018, **29**, 17367–17373.
58 Y. Wang, Q. Guo, N. Tsujii, T. Baba, T. Baba and T. Mori, *ACS Appl. Mater. Interfaces*, 2021, **13**(43), 51245–51254.